

Chapter 4

*Enhanced HER Activity of 1T-SnSe₂ by
Defect Engineering: A DFT Study*

4.1 Introduction

Energy stands as a fundamental necessity for human survival and advancement. Nevertheless, the swift depletion of finite fossil fuel resources and their detrimental impact on the environment has heightened the demand for clean energy alternatives such as biomass, geothermal, solar, hydro, and tidal energy sources [1-4]. Among all the available sources, hydrogen serves as a clean energy source endowed with exceptional characteristics like a high specific energy-to-mass ratio, convenient storage and transport capabilities, and the potential to mitigate harmful emissions [5,6]. However, hydrogen doesn't occur naturally in a readily usable form; nevertheless, it can be generated by various methods worldwide. Among these methods employed for large-scale hydrogen production, water electrolysis stands out as an environmental friendly approach [7-11]. To ensure a continuous supply of hydrogen, it is imperative to have efficient electrocatalysts for the HER that boast high conversion efficiency. While Pt group materials have long been hailed as top-notch HER electrocatalysts, their high cost and limited availability have constrained their application in large-scale hydrogen production [12-14]. Consequently, the exploration of non-precious and abundant materials as catalysts for hydrogen production has emerged as a highly promising avenue. The remarkable characteristics of graphene have paved the way for innovative research, and similar materials with layered two-dimensional (2D) structure exhibit unique electronic and structural qualities [15-18].

2D materials, such as monolayer TMDs [19-27], have exhibited a multitude of intriguing properties, including their potential to replace Pt as HER electrocatalysts. The 2D materials MoS₂ and WS₂ have been the subject of extensive research [28]. Given that SnSe₂ falls within the category of TMDs, it's reasonable to anticipate that it shares similar structural properties with other members of this group, such as MoS₂ and WS₂. These materials have

garnered significant attention recently as promising candidates for electrocatalysis due to their cost-effective production methods and superior electrocatalytic performance [29]. SnSe₂, stands out as an n-type semiconductor featuring a narrow indirect bandgap spanning 0.75 eV. With these characteristics it is a promising candidate for various electronic device applications [30]. The synthesis of 2D SnSe₂ is conveniently achievable through techniques such as molecular beam epitaxy [31] and chemical vapor deposition [32], owing to the weak van der Waals interactions that hold its layers together. Moreover, 2D SnSe₂ is an economically viable, environmentally friendly, and non-toxic material, offering considerable potential in optoelectronics and nanoelectronics devices, including thermoelectrics [33], catalysis [29], lithium-ion batteries [34], field effect transistors [35] solar cells, and film electrodes [36]. Monolayer MX₂ boasts a distinctive X–Sn–X sandwich-like structure, which can be easily crafted using traditional mechanical exfoliation methods [37,38]. Here, M denotes the transition metal element, and X signifies a chalcogen element, which can be sulfur (S), selenium (Se), or tellurium (Te). These 2D TMDs exhibit a diverse range of physical and chemical properties, including metallic, half-metallic, semiconducting, magnetic, and catalytic behaviour.

Defect chemistry encompasses different types of imperfections, including edge defects, topological defects, vacancies, and dopant-derived defects in 2D materials. These defects hold significant importance in electrocatalysis because they often serve as active sites actively participating in chemical reactions. Additionally, defects can influence the electronic structure of active sites and promote the exposure of more catalytic sites to the electrolyte [39-42]. Consequently, defect engineering has emerged as a highly promising approach for finely tuned electrocatalytic performance [43,39-40]. For instance, Sun et al. [44] managed to modify the magnetic ground state and optical characteristics of a SnS₂ monolayer through Zn doping. Tian et al. [45] altered the magnetic ground state and optical properties of a CrS₂ monolayer through

vacancy defects. They conducted a study focusing on the electronic, magnetic, and optical characteristics of single-layer CrS₂, both with and without vacancy defects. Among the various vacancy types considered, it was found that the S vacancy exhibited the highest energy favourability, surpassing Cr vacancy, S₂ double vacancy, and CrS double vacancy. The presence of vacancies induced defect states within the original band gap, leading to a notable reduction in the band gaps of single-layer CrS₂ when compared to the defect-free structure. In its pristine state, single-layer CrS₂ behaves as a nonmagnetic direct band gap semiconductor. However, introducing either a Cr vacancy or CrS double vacancy transforms it into a magnetic semiconductor. Interestingly, the S vacancy and S₂ double vacancy still maintain their nonmagnetic semiconductor nature but exhibit reduced band gaps. Moreover, the introduction of vacancies in single-layer CrS₂ resulted in higher static dielectric constants and static refractive indices compared to the perfect CrS₂ due to the narrowed band gaps. Additionally, the first primary absorption peak was observed to weaken, while the other two main peaks showed significant enhancement in single-layer CrS₂ with vacancies [45]. Niar et al. [46] reported that point defects induce a magnetic ground state in graphene. Feng et al. [47] investigated the impact of vacancies in a MoS₂ monolayer, demonstrating that vacancies can influence its optical and magnetic properties. Their research findings indicate that the band structure and band gap of a pristine monolayer of MoS₂ align well with existing experimental and theoretical data. Upon closer examination of the structure, it was observed that ions surrounding Mo vacancies exhibited an outward relaxation, while those surrounding S vacancies displayed a slight inward relaxation. In terms of electronic properties, defective monolayer MoS₂ demonstrated smaller band gaps compared to the defect-free counterpart. Introducing a neutral S vacancy caused the monolayer MoS₂ to shift from having a direct to an indirect band gap. Mo vacancies introduced acceptor-like levels and resulted in p-type conductivity, while S vacancies introduced donor-like levels leading to n-type conductivity.

Furthermore, with increasing charge states of the vacancies, the band gaps diminished, and the defect energy levels became more profound. Moreover, the static dielectric constants of monolayer MoS₂ with Mo vacancies decreased as the charge states of the vacancies increased, whereas the static dielectric constants of monolayer MoS₂ with S vacancies increased under the same conditions [47]. Sun et al. [48] induced magnetism in a SnS₂ monolayer through intrinsic defects. Among the various intrinsic defects that could occur, it was found that S vacancies are the most energetically favoured defects in conditions where there is an excess of tin (Sn). Conversely, under S-rich conditions, S-on-Sn anti-site defects are more likely to form. Notably, S-on-Sn anti-site defects can confer p-type semiconductor characteristics to the material. Furthermore, defects such as Sn vacancies, Sn-on-S anti-sites, and the adsorption of S atoms on the top of S atoms from the upper triple layer were identified as triggers for magnetism in the material. This magnetism primarily arises from the nearest-neighbour S atoms in proximity to the Sn vacancy, Sn substitutional atom, and S adatom, respectively. What's intriguing is that at room temperature, it becomes possible to achieve ferromagnetism in monolayer SnS₂ through the introduction of S adsorption on the top of S atoms from the upper triple layer defects. These findings open up new avenues for exploring magnetic nanomaterials based on monolayer SnS₂ [48]. While Wang et al. [49] introduced magnetism into a pristine ZrS₂ monolayer via structural defects. Zhou et al. [50] employed DFT to delve into the properties of defective MoS₂ with varying numbers of S vacancies. With low concentration of S vacancies, it was observed that these vacancies tended to aggregate rather than disperse evenly across the material. Conversely, at higher vacancy concentrations, preference for a combination of local point defects and clustered vacancy chains. This coupling between S vacancies resulted in several notable effects. First, it led to a reduction in the band gap of the material, making it more conductive. Second, it enhanced the strength of Mo-H adsorption on the surface. Importantly, it was identified that the optimal HER activity occurred

at a vacancy concentration below 12.50%. The research provides valuable insights at the atomic level, shedding light on the role of S vacancies in shaping the HER performance of MoS₂.

In the present work, we have systematically optimized 1T- SnSe₂ monolayer and incorporated various defects namely, mono-selenide vacancy (V_{se}), di-selenide vacancy (V_{Se_2}), vacancy complex of Sn and nearby three selenide (V_{SnSe_3}) and vacancy complex of Sn and nearby three di-selenide pairs (V_{SnSe_6}). The structural, electronic and catalytic properties of the pristine and defected structures are vividly discussed.

4.2 Computational Methods

In this research, we conducted all the necessary computations using state-of-the-art first-principles DFT techniques, which were implemented through the Quantum Espresso code [51]. To account for the exchange-correlation interaction, we employed the widely recognized Perdew-Burke-Ernzerhof (PBE) generalized gradient approximation (GGA) [52]. Furthermore, we incorporated Grimme's dispersion correction (D3) into our calculations to ensure the accuracy of adsorption energy calculations for hydrogen adsorption on 1T-SnSe₂ [53]. A 5x5x1 supercell was considered for 1T-SnSe₂ to ensure sufficient area to create the defects and obtain acceptable results. To achieve convergence within specified criteria, we set the kinetic energy cut-off at 45 Rydberg. Additionally, we introduced a 21 Å thick vacuum layer perpendicular to the monolayer to prevent interactions between successive layers. In terms of sampling the reciprocal space, we used a dense 5x5x1 grid based on the Monkhorst-Pack scheme [54]. The Marzari-Vanderbilt smearing has been incorporated into the required calculations. Throughout the calculations, we maintained an energy convergence threshold of 10⁻⁵ eV, and self-consistently iterated until the maximum Hellmann-Feynman forces acting on individual atoms fell below 0.001 eV/Å.

The study investigates the HER activity in pristine and defective monolayers of SnSe₂ applying the Sabatier principle as a guiding concept [1-4]. The Sabatier principle essentially suggests that the interaction between catalysts and intermediates should be neither too strong nor too weak. At equilibrium conditions, the effectiveness of the HER activity on a given surface is determined by the exchange current density, which is linked to the change in Gibbs free energy of H adsorption (ΔG^H) at a pH of 0. Pt, a renowned catalyst, exhibits a ΔG^H value close to zero. Consequently, for exceptional catalytic HER activity, ΔG^H should approach zero or be very close to it. When ΔG^H is overly positive, it indicates weak binding of H to the surface, making the adsorption step challenging. Conversely, if ΔG^H is highly negative, it implies strong binding of H to the surface, making the desorption step difficult. Thus, achieving an optimal ΔG^H is a crucial condition for excellent catalytic HER activity [55-57].

4.3 Results and Discussion

Before evaluating the Volmer reaction mechanism, we have optimized 5x5x1 supercell of SnSe₂ and defected SnSe₂ monolayers. The created defects are named as, mono-selenide vacancy (V_{Se}), di-selenide vacancy (V_{Se_2}), vacancy complex of Sn and nearby three selenide (V_{SnSe_3}) and vacancy complex of Sn and nearby three di-selenide pairs (V_{SnSe_6}). The compound stabilizes in 1T phase with the space group P-3m1 which has CdI₂ as its parent prototype. The compound has octahedral coordination where Sn atoms are surrounded by the Se atom which is similar to the SnS₂ compound. The lattice constant of unit cell is reported to be 3.823 Å experimentally as well as theoretically [58,59]. The lattice constant and bond-length of 5x5x1 supercell are 19.17 Å and 2.73 Å which are in good accordance with previous reported studies. The 5x5x1 size of supercell was selected to study the effect of defects which provide sufficient area for various defects. The introduction of defects does minor changes in the structural

properties of monolayer. The optimized structures of pristine as well as defected SnSe₂ monolayers are pictorially represented in **Figure 4.1**.

Firstly, we have evaluated the Volmer reaction over pristine and defected SnSe₂ at all possible sites. The stable configurations are considered the one's that provide minimum value for ΔG^H . In case of pristine SnSe₂, it is observed that the configuration providing least ΔG^H value is the one where H is adsorbed at Sn and Se site. In case of V_{Se} defected SnSe₂, the least ΔG^H values are obtained for Sn, Se and hollow sites. For V_{Se_2} defected SnSe₂, the least ΔG^H values are obtained for Sn, Se and hollow sites. Considering the case of V_{SnSe_3} , the least ΔG^H values is the one in which H was adsorbed at the two Se and hollow sites. For V_{SnSe_6} , the least ΔG^H values are derived for Sn and hollow sites. The optimized structures for H adsorption on pristine and defected SnSe₂ on various sites are presented in **Figure 4.2**.

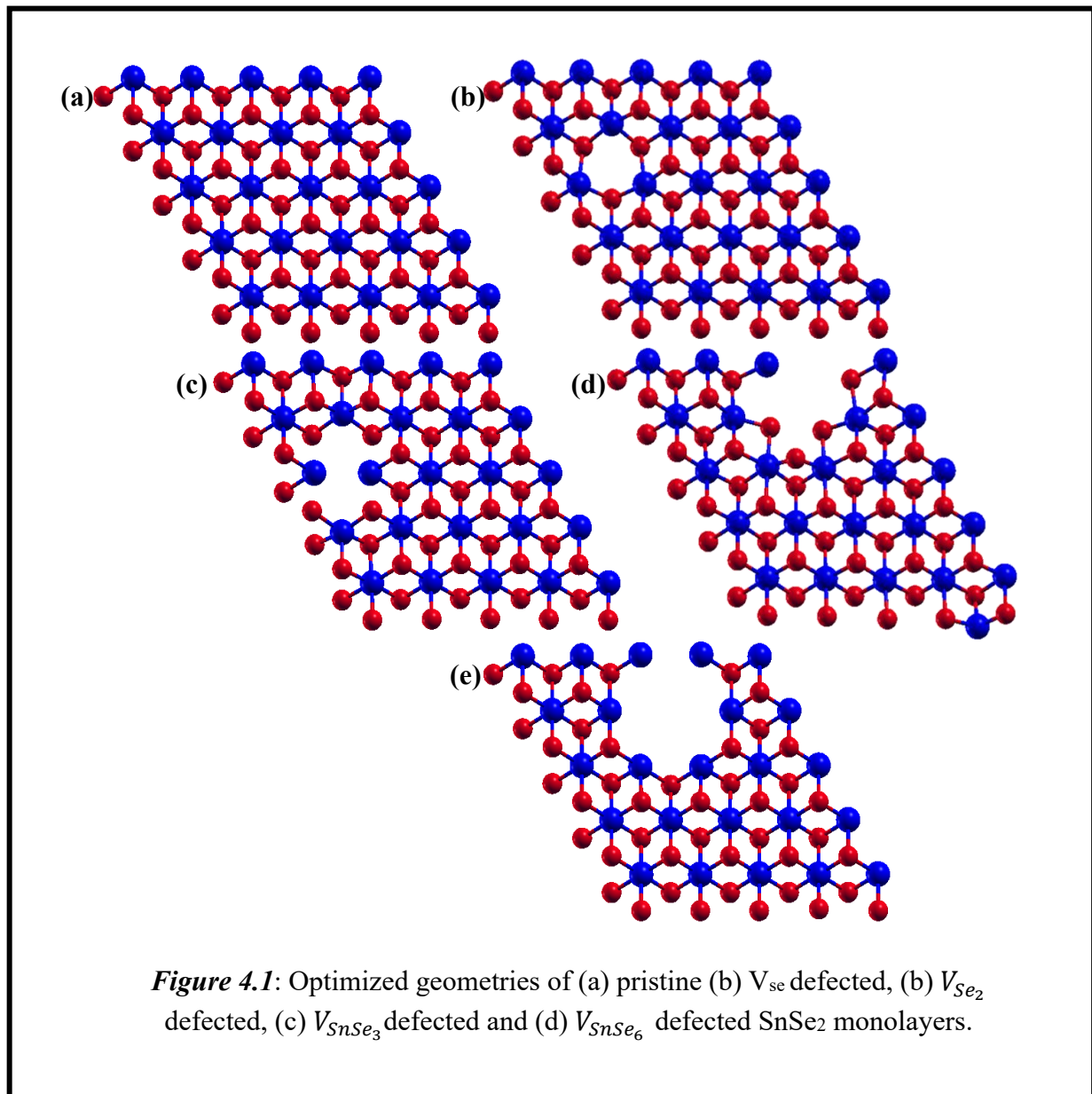
It is observed in the case of pristine SnSe₂, H binds with the Se atom for both cases. In case of V_{Se} defect, H atom binds with Se atom for Sn and Se-site adsorption and in case of hollow site, it bonds with the Sn atom. For V_{Se_2} , the H atom binds with Se atom for the Sn and Se adsorption site while it is adsorbed at the bridge site of Sn atoms in case of hollow site adsorption. For V_{SnSe_3} , the H atom prefers to bind with the Se atoms in all three adsorption sites. In case of V_{SnSe_6} , the H atom in case of Sn-site adsorption prefers to bind with Se atom while in case of hollow site adsorption, it prefers the bind with the Sn atom.

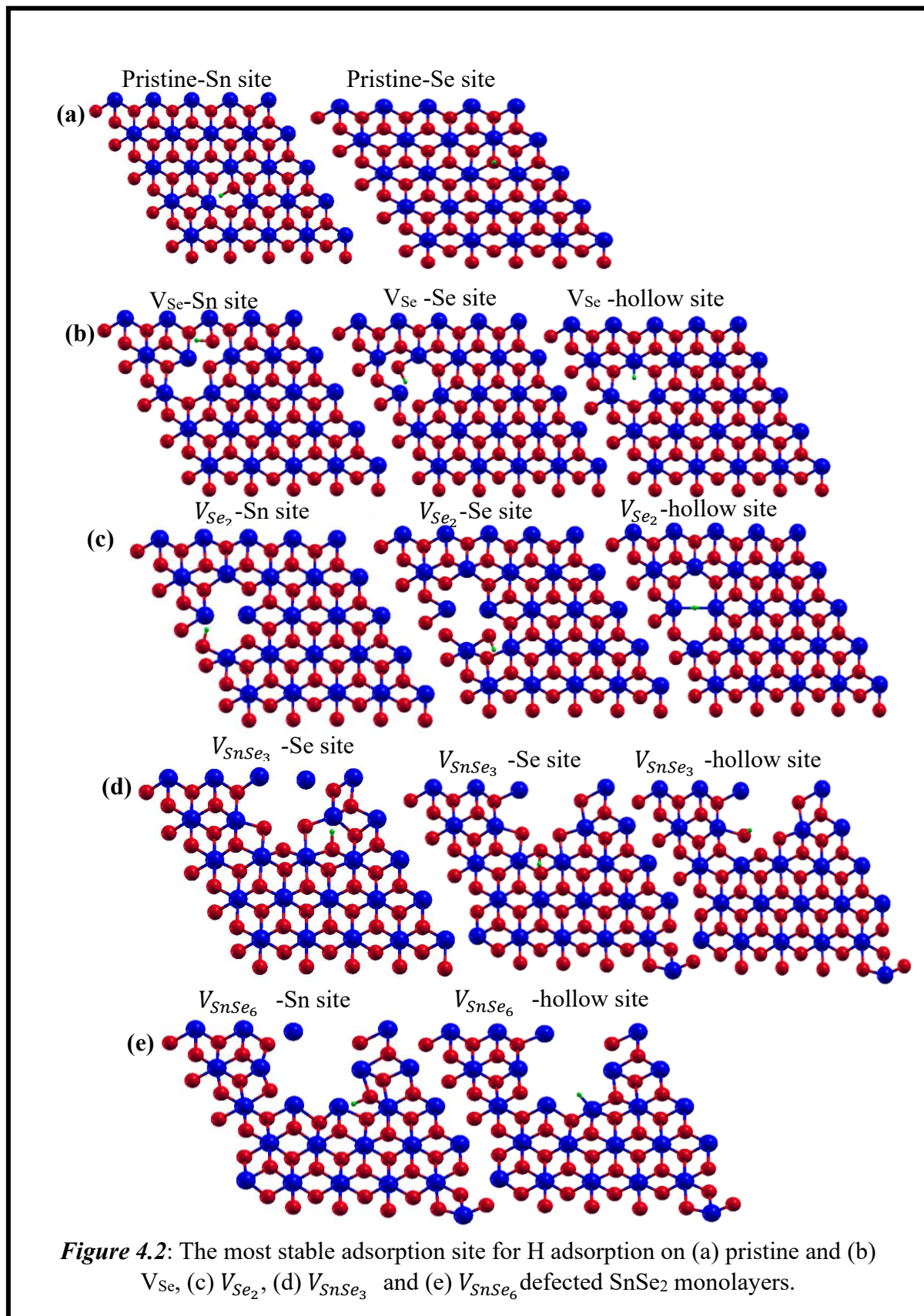
It is reported in various studies that the basal plane shows inactivity as compared to the edge sites of TMDs [60]. Here, in order to discuss the catalytic efficiency of pristine as well as defected SnSe₂, we have calculated ΔE_{ads}^H and ΔG^H . The calculated values of ΔE_{ads}^H and ΔG^H are presented in **Table 4.1**. It is observed that various defects impact the H binding to the surface differently. Here, we observe that in case of V_{Se} defect, the ΔG^H for all three adsorption sites show positive values that can be attributed to the fact that the interactions between H and SnSe₂

basal plane are still too weak. It can be deduced that the basal plane remains insufficient to establish the necessary bonds required to facilitate the proton-electron transfer process. In case of V_{Se_2} defect, the ΔG^H values show a similar trend for positive values that concludes the weak interaction between H and basal plane of SnSe₂. Whereas, in case of V_{SnSe_3} defect, we observe that the H adsorption on all three sites provide ΔG^H value approaching to zero which indicates stability as HER catalysts. Also, in case of V_{SnSe_6} defect, we observe that ΔG^H shows highly negative values for Sn site, determining the strong interaction which can result in difficulty in desorption at the end of the process and for hollow site ΔG^H is close to zero which makes it suitable for HER activity. It is observed that in case of pristine SnSe₂, the ΔG^H value for Sn adsorption site (0.76 eV) is better as compared to Se site which yields a value of 0.88 eV but indicating inertness for HER activity. The defect engineering is employed to enhance the catalytic efficiency which should also be observed in the obtained data. In case of V_{Se} defect, the hollow site provides a satisfactory ΔG^H value of 0.40 eV as compared to Sn and Se site which has value 0.54 and 0.48 eV respectively. In case of V_{Se_2} defect the ΔG^H value shows that the Se site is favourable for catalysis as compared to Sn site and hollow site. In case of V_{SnSe_3} defect, the Se sites as well as hollow sites provide good ΔG^H value of 0.27, -0.22 and 0.19 eV respectively. Lastly, V_{SnSe_6} defect has better catalytic efficiency for H adsorption at hollow site as compared to Sn site. Among all the defects it is evident that V_{SnSe_3} hollow site is the best candidate for HER followed by V_{SnSe_3} and V_{SnSe_6} Se site and hollow site respectively. The obtained values clearly illustrate that within the defect regions, the ΔG^H values associated with H adsorption sites are significantly lower compared to those of the pristine SnSe₂ basal plane surface, which has a Gibbs free energy of 0.76 eV and 0.88 eV for Sn and Se sites respectively. This observation strongly suggests that these structural defects have the capability to disrupt the inherent stability of the basal plane and, as a result,

improve the interaction between H atoms and the adsorption sites. Hence, defects lead to the significant improvement in the HER activity of monolayers.

Understanding the chemical properties of materials is contingent upon the fundamental electronic structure beneath. Analyzing the PDOS can provide





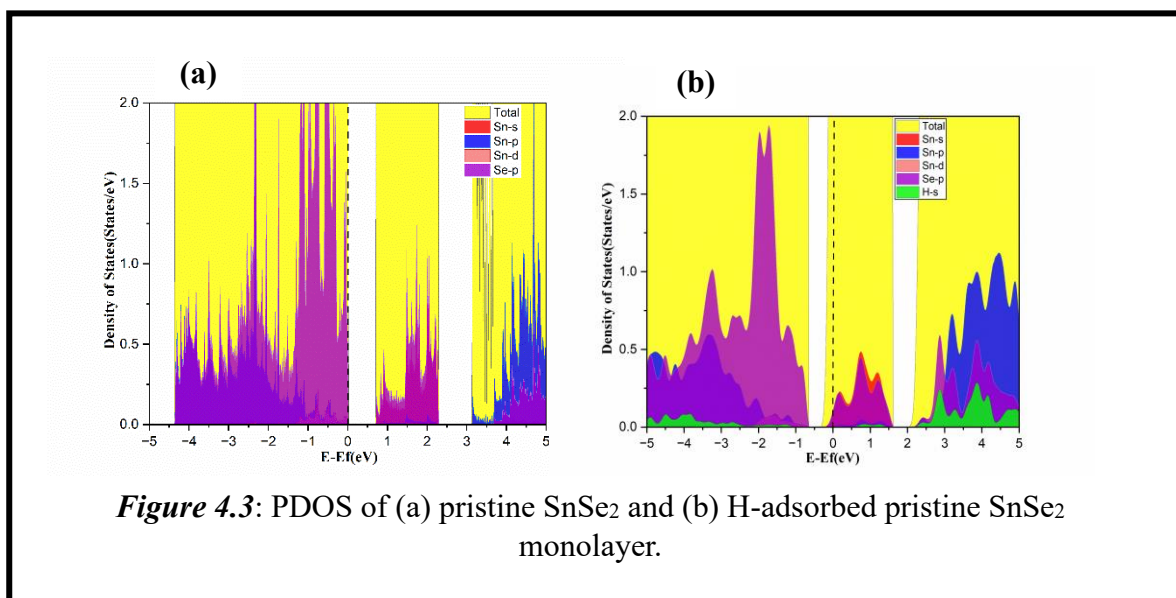
valuable insights into the interaction between H atoms and defects in SnSe₂, shedding light on the varying HER activities exhibited by these imperfect structures. The PDOS plots for pristine and H-adsorbed pristine SnSe₂ are shown in **Figure 4.3**. The PDOS plots for H adsorption providing better catalytic efficiency are discussed further.

Table 4.1: Calculated ΔE_{ads}^H and ΔG^H of HER activity over pristine and defected SnSe₂ monolayers.

System	Adsorption site	ΔE_{ads}^H (eV)	ΔG^H (eV)
Pristine SnSe₂	Sn	0.52	0.76
	Se	0.64	0.88
(V_{Se}) defect	Sn	0.30	0.54
	Se	0.24	0.48
	Hollow	0.16	0.40
(V_{Se₂) defect}	Sn	0.27	0.51
	Se	0.21	0.45
	Hollow	0.48	0.72
(V_{SnSe₃) defect}	Se	0.02	0.26
	Se	-0.46	-0.22
	Hollow	-0.05	0.19
(V_{SnSe₆) defect}	Sn	-1.11	-0.87
	Hollow	-0.46	-0.22

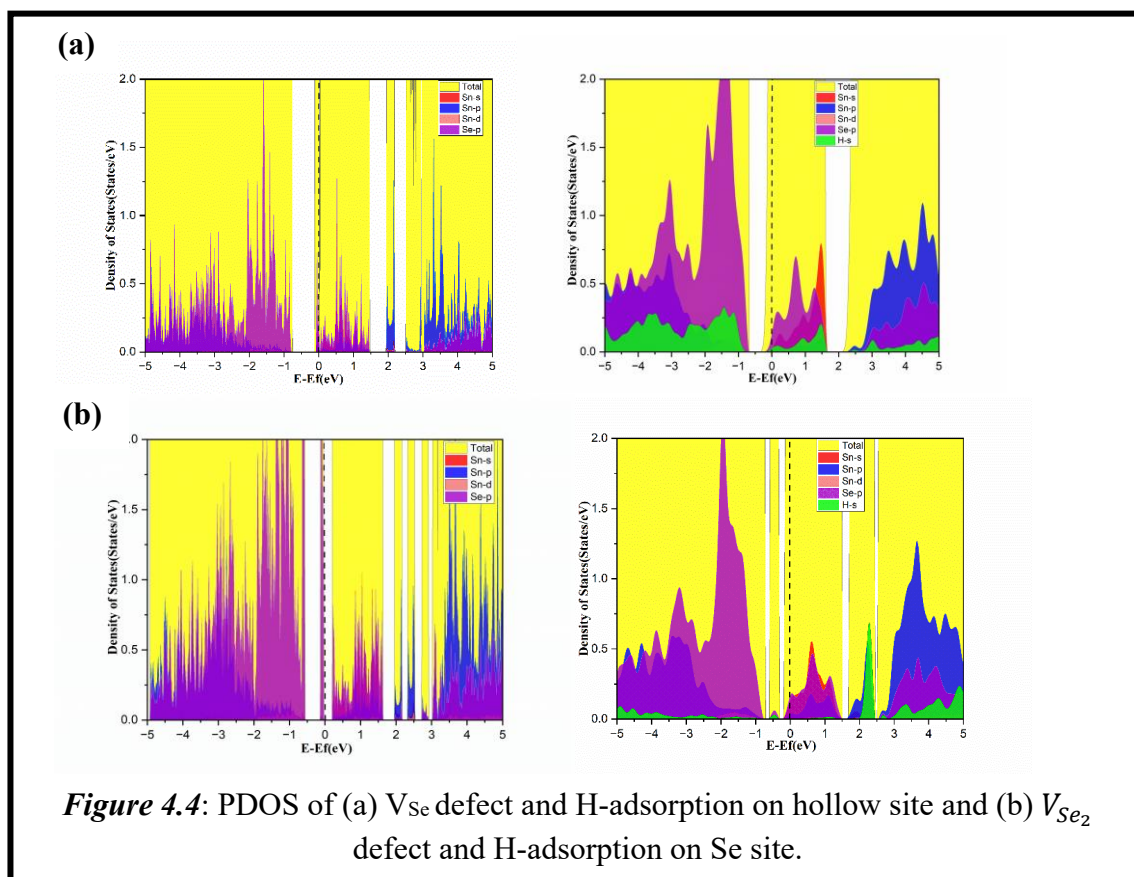
Here, in case of pristine SnSe₂, we can observe that it is semiconductor in nature and has band gap of 0.75 eV which is in accordance with previous reported studies [61]. Moreover, the PDOS plot denotes that the contribution of Se-p orbital is dominant towards valence band followed by Sn-p orbital in the same. The contribution of Sn-s and d orbital is negligible. The

PDOS analysis is carried out to uncover the perturbations in electronic properties of SnSe₂ monolayer after H adsorption. The PDOS plots reveal that the H adsorption in case of pristine alters the band gap converting the system from semiconducting to metallic. This reveals that



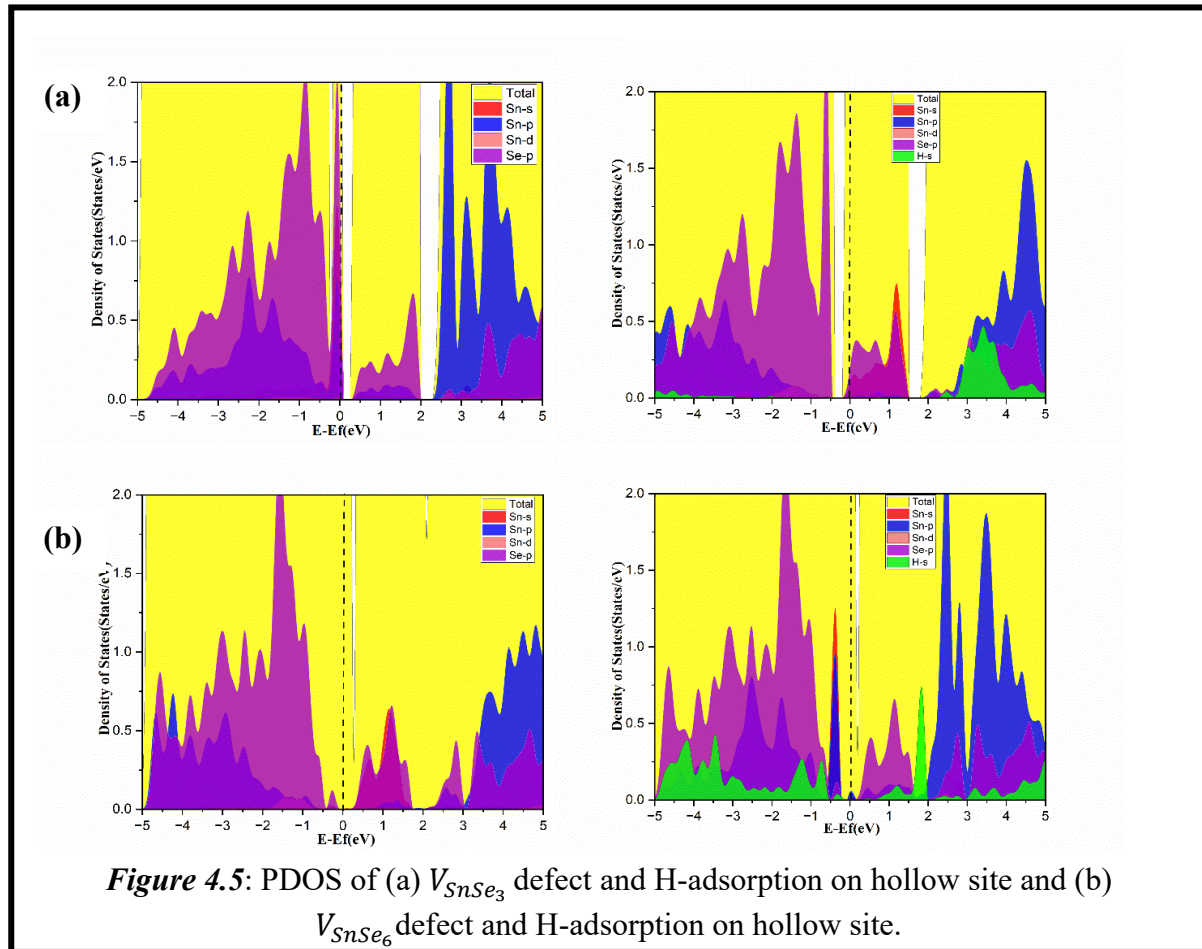
the conductivity of SnSe₂ monolayer is improved after H adsorption. We can see that H 1s orbital profoundly hybridizes with the p orbital of the Se atom. Their bonding states locate at the energy range from -2.5 eV to -5 eV. For the corresponding antibonding states, no contribution is observed near the Fermi energy level, most of them distribute above ranging from 2.2 eV to 5 eV. **Figure 4.4** below shows the comparison of PDOS for V_{Se} and V_{Se_2} defects and hollow site and Se-site H-adsorption. In case of V_{Se} defect SnSe₂, we observe that the contribution of Se-p is dominant towards valence band whereas the contribution of Sn-p orbital is dominant towards conduction band. After H-adsorption the contribution of Sn-s orbital towards conduction band is visible. There is a small peak of H contribution near the Fermi level but the higher peak is observed towards valence band indicating its sufficient interaction with the surface. This is attributed to the interaction between them. In case of V_{Se_2} defected SnSe₂, monolayer shows a semiconducting nature. The contribution of Se-p orbital is dominant

towards valence band whereas for Sn-p it is dominant towards the conduction band. The H-adsorption makes the defected system metallic in nature and contributes more towards conduction band away from Fermi level indication interaction with the system and physisorption nature.



The PDOS plots for both V_{Se} defected SnSe₂ and V_{Se_2} defected SnSe₂, reveals that the H adsorption in case of pristine alters the band gap from semiconducting to metallic. This reveals that the conductivity of SnSe₂ monolayer is improved after defect creation, which is useful for the electron transport in during HER activity. We can see that H 1s orbital profoundly hybridizes with the p orbital of the Sn atom in case of V_{Se} defect and H 1s orbital profoundly hybridizes with the p orbital of the Se atom in case of V_{Se_2} defect. The bonding states in case of V_{Se} defect locate at the energy range from -1 eV to -5 eV. For the corresponding antibonding states, contribution is observed near the Fermi level, distributed from 0 eV to 1.5 eV and above

the Fermi level ranging from 2.9 eV to 5 eV. The bonding states in case of V_{Se_2} defect locate at the energy range from -1.5 eV to -5 eV. For the corresponding antibonding states, no contribution is observed near the Fermi level and above the Fermi level ranging from 2 eV to 5 eV. **Figure 4.5** denotes the PDOS for V_{SnSe_3} and V_{SnSe_6} SnSe₂ as well as H-adsorption on hollow sites.



Here, as observed in case of V_{SnSe_3} defected SnSe₂, the contribution of Se-p is dominant towards valence band whereas the contribution of Sn-p is dominant towards the conduction band. The defect shows a semiconducting nature which becomes metallic after H-adsorption. The contributions of Se-p towards valence band remains the same but detriment is observed in Sn-p contribution towards conduction band. In case of V_{SnSe_6} defected SnSe₂, the contribution

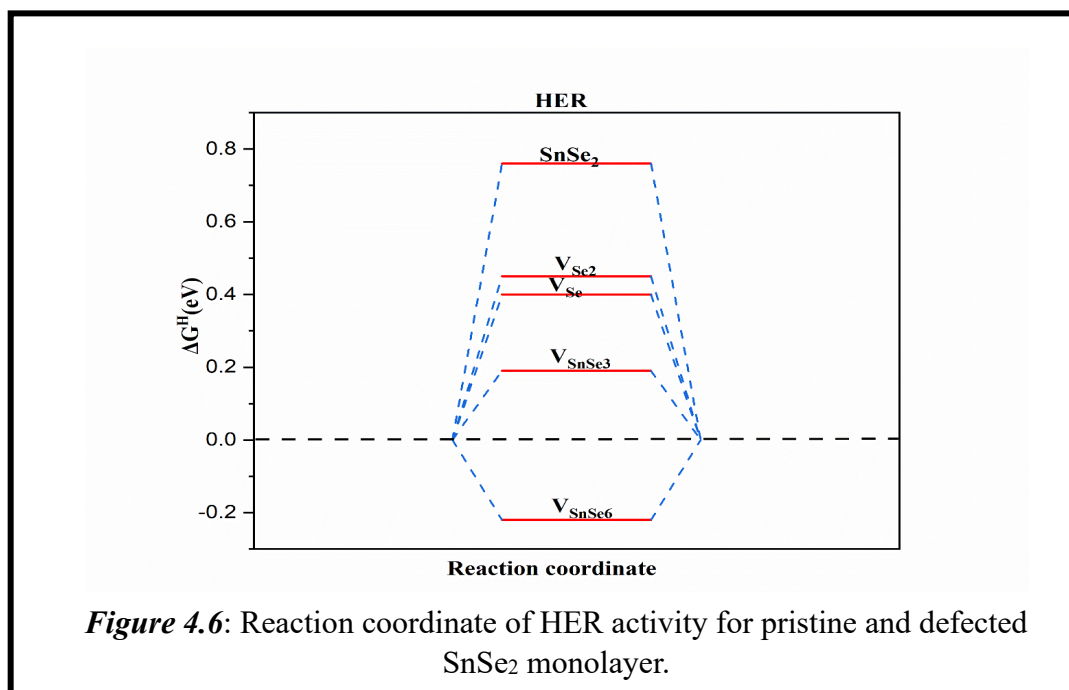
of Se-p shows dominance in valence band whereas Sn-p shows towards conduction band. The system shows semiconducting nature which converts to metallic upon H-adsorption. After H-adsorption a peak in the Sn-s orbital contribution towards valence band is evident. There is an increment in the Sn-p contribution towards the conduction band after H-adsorption. The H-adsorption makes the defected system contribute more towards conduction band away from Fermi level indication interaction with the system and physisorption nature. The PDOS plots for both V_{SnSe_3} defect SnSe₂ and V_{SnSe_6} defect SnSe₂, reveal that the H adsorption in case of pristine alters the band gap converting the system to metallic. We can see that H 1s orbital profoundly hybridizes with the p orbital of the Se atom in case of V_{SnSe_3} defect and H 1s orbital profoundly hybridizes with the p orbital of the Sn atom in case of V_{SnSe_6} defect. The bonding states in case of V_{SnSe_3} defect locate at the energy range from -4 eV to -5 eV. For the corresponding antibonding states, no contribution is observed near the Fermi level, and above the Fermi level ranging from 2.3 eV to 5 eV. The bonding states in case of V_{SnSe_6} defect locate at the energy range from 0 eV to -5 eV. For the corresponding antibonding states, no contribution is observed near the Fermi level and above the Fermi level ranging from 0.8 eV to 5 eV. **Figure 4.6** shows the reaction coordinate plot for HER of pristine and defected SnSe₂. The reaction coordinate plot determines the HER activity. The value of ΔG^H close to the Fermi level i.e zero, shows better catalytic activity as compared to others. In this case, it is evident from the plot that V_{SnSe_3} and V_{SnSe_6} show best catalytic efficiency as compared to other defected systems. **Table 4.2** presents the changes in ΔG^H for various TMDs before and after the introduction of defects. Specifically, we observe variations in ΔG^H for CoTe₂, FeS₂, CrS₂, CrTe₂, CrSe₂, NiS₂, VS₂, TaS₂, NbS₂, and NiTe₂ when defects involving transition metals (TM)

Table 4.2: The comparison of ΔG^H of all stable 2D-TMDs. (Ref. [62])

TMX ₂	(TMX ₂) $\Delta G_{H^*}(\text{eV})$	(TM-vacancy) $\Delta G_{H^*}(\text{eV})$	(X-vacancy) $\Delta G_{H^*}(\text{eV})$
CoTe ₂	-0.17	-0.15	-0.21
FeS ₂	0.13	-0.25	-0.01
CrS ₂	-0.11	-0.2	0.18
CrTe ₂	-0.14	-0.19	0.28
CrSe ₂	-0.11	-0.19	0.03
NiS ₂	-0.06	-0.22	-0.25
VS ₂	0.08	0.15	0.25
TaS ₂	0.18	-0.23	-0.1
NbS ₂	0.21	-0.18	0.23
NiTe ₂	0.21	-0.12	0.14

or chalcogen (X) vacancies are created. For CoTe₂, initially, the ΔG^H value is -0.17 eV. After introducing a TM vacancy, it becomes -0.15 eV, and after X vacancy, it decreases further to -0.21 eV. In the case of FeS₂, the ΔG^H value before defect creation is 0.13 eV. However, after introducing a TM vacancy, it decreases significantly to -0.25 eV, and after X vacancy, it becomes -0.01 eV, indicating a notable improvement in catalytic efficiency. For CrS₂, the initial ΔG^H value is -0.11 eV. Moreover, introducing X vacancy results in a higher ΔG^H of 0.18 eV, indicating an unexpected change in catalytic behaviour. In the case of CrTe₂, the ΔG^H value increases after both TM and X vacancies are created, suggesting a decrease in catalytic efficiency. Similarly, CrSe₂ exhibits an improved ΔG^H value after the introduction of X vacancy, indicating enhanced catalytic potential. NiS₂ and VS₂ follow a similar trend to CrTe₂, with an increase in ΔG^H after both TM and X vacancies are created, suggesting a decrease in catalytic efficiency. For TaS₂, the ΔG^H value shows positive results after the introduction of vacancy defects, indicating improved catalytic efficiency. NbS₂ displays a higher ΔG^H value after the creation of X vacancy, suggesting an enhancement in its catalytic properties. Lastly,

NiTe₂ demonstrates an improvement in catalytic efficiency after the creation of both TM and X vacancies. These observations highlight the diverse responses of different TMDs to defect creation, which can have a significant impact on their catalytic properties.



4.4 Conclusions

In our investigation, we explored the structural and electronic characteristics of pristine and defected SnSe₂, along with HER activity. To assess the catalytic activity of these materials, we computed ΔE_{ads}^H and ΔG^H for H adsorption. In the case of pristine SnSe₂, we observe that the ΔG^H values are far from an ideal catalyst which indicates inertness towards HER activity. To enhance the catalytic efficiency further, we introduced various defects into these materials, which had a profound impact on their electronic properties. For the V_{Se} defect, hollow site adsorption results in a satisfactory ΔG^H value of 0.40 eV, whereas the Sn and Se sites have values of 0.54 eV and 0.48 eV, respectively. In the case of V_{Se_2} defect, the ΔG^H values indicate that the Se site is more favourable for catalysis compared to the Sn site and the hollow site. Considering the V_{SnSe_3} defect, both Se sites and hollow sites exhibit favourable ΔG^H values of

0.27 eV, -0.22 eV, and 0.19 eV, respectively. Lastly, in the case of V_{SnSe_6} defect, the catalytic efficiency for H adsorption at the hollow site surpasses that at the Sn site. Among all the defects, it becomes evident that the V_{SnSe_3} hollow site is the most promising candidate for the HER, followed by the V_{SnSe_3} and V_{SnSe_6} Se sites and hollow sites, respectively. In general, defects significantly modulates the HER performance of SnSe₂ monolayer and approaches in range of ideal values in certain cases. We are hoping that our DFT based prediction motivates the experimentalists to design SnSe₂ based efficient HER catalyst.

References

1. B. Dunn, H. Kamath and J.-M. Tarascon, *Science (1979)*, 2011, **334**, 928–935.
2. Z. Yang, J. Zhang, M. C. W. Kintner-Meyer, X. Lu, D. Choi, J. P. Lemmon and J. Liu, *Chem Rev*, 2011, **111**, 3577–3613.
3. Q. Zhu, Y. Qu, D. Liu, K. W. Ng and H. Pan, *ACS Appl Nano Mater*, 2020, **3**, 6270–6296.
4. P. A. Owusu and S. Asumadu-Sarkodie, *Cogent Eng*, 2016, **3**, 1167990.
5. I. Dincer and C. Acar, *Int J Hydrogen Energy*, 2015, **40**, 11094–11111.
6. L. A. Burton, T. J. Whittles, D. Hesp, W. M. Linhart, J. M. Skelton, B. Hou, R. F. Webster, G. O’Dowd, C. Reece, D. Cherns, D. J. Fermin, T. D. Veal, V. R. Dhanak and A. Walsh, *J Mater Chem A Mater*, 2016, **4**, 1312–1318.
7. Z. Xu, Z. Ao, D. Chu, A. Younis, C. M. Li and S. Li, *Sci Rep*, 2014, **4**, 6450.
8. A. Kudo and Y. Miseki, *Chem. Soc. Rev.*, 2009, **38**, 253–278.
9. S. U. M. Khan, M. Al-Shahry and W. B. Ingler, *Science (1979)*, 2002, **297**, 2243–2245.
10. W.-F. Chen, S. Iyer, S. Iyer, K. Sasaki, C.-H. Wang, Y. Zhu, J. T. Muckerman and E. Fujita, *Energy Environ Sci*, 2013, **6**, 1818.
11. W.-F. Chen, J. T. Muckerman and E. Fujita, *Chemical Communications*, 2013, **49**, 8896.
12. J. O. M. Bockris, I. A. Ammar and A. K. M. S. Huq, *J Phys Chem*, 1957, **61**, 879–886.
13. R. Parsons, *Transactions of the Faraday Society*, 1960, **56**, 1340.
14. M. G. Walter, E. L. Warren, J. R. McKone, S. W. Boettcher, Q. Mi, E. A. Santori and N. S. Lewis, *Chem Rev*, 2010, **110**, 6446–6473.
15. K. S. Novoselov, A. K. Geim, S. V. Morozov, D. Jiang, M. I. Katsnelson, I. V. Grigorieva, S. V. Dubonos and A. A. Firsov, *Nature*, 2005, **438**, 197–200.

16. V. P. Gusynin and S. G. Sharapov, *Phys Rev Lett*, 2005, **95**, 146801.
17. M. Khalid Butt, H. Muhammad Zeeshan, V. An Dinh, Y. Zhao, S. Wang and K. Jin, *Comput Mater Sci*, 2021, **197**, 110617.
18. N. M. Peres, *Rev. Mod. Phys.*, 2010, **82**, 2673-2700.
19. K. S. Novoselov, D. Jiang, F. Schedin, T. J. Booth, V. V. Khotkevich, S. V. Morozov and A. K. Geim, *Proceedings of the National Academy of Sciences*, 2005, **102**, 10451–10453.
20. H. Li, L. Pan, T. Lu, Y. Zhan, C. Nie and Z. Sun, *Journal of Electroanalytical Chemistry*, 2011, **653**, 40–44.
21. K. S. Novoselov, A. K. Geim, S. V. Morozov, D. Jiang, Y. Zhang, S. V. Dubonos, I. V. Grigorieva and A. A. Firsov, *Science (1979)*, 2004, **306**, 666–669.
22. L. Yang, K. Majumdar, H. Liu, Y. Du, H. Wu, M. Hatzistergos, P. Y. Hung, R. Tieckelmann, W. Tsai, C. Hobbs and P. D. Ye, *Nano Lett*, 2014, **14**, 6275–6280.
23. E. Scalise, M. Houssa, G. Pourtois, V. Afanas'ev and A. Stesmans, *Nano Res*, 2012, **5**, 43–48.
24. N. Perea-López, A. L. Elías, A. Berkdemir, A. Castro-Beltran, H. R. Gutiérrez, S. Feng, R. Lv, T. Hayashi, F. López-Urías, S. Ghosh, B. Muchharla, S. Talapatra, H. Terrones and M. Terrones, *Adv Funct Mater*, 2013, **23**, 5511–5517.
25. Y. Gao, Z. Liu, D.-M. Sun, L. Huang, L.-P. Ma, L.-C. Yin, T. Ma, Z. Zhang, X.-L. Ma, L.-M. Peng, H.-M. Cheng and W. Ren, *Nat Commun*, 2015, **6**, 8569.
26. Y. Huang, E. Sutter, J. T. Sadowski, M. Cotlet, O. L. A. Monti, D. A. Racke, M. R. Neupane, D. Wickramaratne, R. K. Lake, B. A. Parkinson and P. Sutter, *ACS Nano*, 2014, **8**, 10743–10755.
27. H. S. S. Ramakrishna Matte, A. Gomathi, A. K. Manna, D. J. Late, R. Datta, S. K. Pati and C. N. R. Rao, *Angewandte Chemie International Edition*, 2010, **49**, 4059–4062.
28. A. N. Inamdar, N. N. Som, A. Pratap and P. K. Jha, *Int J Hydrogen Energy*, 2020, **45**, 18657–18665.
29. S. Dong and Z. Wang, *Beilstein Journal of Nanotechnology*, 2018, **9**, 1820–1827.
30. E. P. Mukhokosi, S. B. Krupanidhi and K. K. Nanda, *Sci Rep*, 2017, **7**, 15215.
31. Y. W. Park, S.-K. Jerng, J. H. Jeon, S. B. Roy, K. Akbar, J. Kim, Y. Sim, M.-J. Seong, J. H. Kim, Z. Lee, M. Kim, Y. Yi, J. Kim, D. Y. Noh and S.-H. Chun, *2d Mater*, 2016, **4**, 014006.
32. X. Zhou, L. Gan, W. Tian, Q. Zhang, S. Jin, H. Li, Y. Bando, D. Golberg and T. Zhai, *Advanced Materials*, 2015, **27**, 8035–8041.

33. B.-Z. Sun, Z. Ma, C. He and K. Wu, *Physical Chemistry Chemical Physics*, 2015, **17**, 29844–29853.
34. F. Zhang, C. Xia, J. Zhu, B. Ahmed, H. Liang, D. B. Velusamy, U. Schwingenschlögl and H. N. Alshareef, *Adv Energy Mater*, 2016, **6**.
35. X. Yan, C. Liu, C. Li, W. Bao, S. Ding, D. W. Zhang and P. Zhou, *Small*, 2017, **13**.
36. J. Choi, J. Jin, I. G. Jung, J. M. Kim, H. J. Kim and S. U. Son, *Chemical Communications*, 2011, **47**, 5241.
37. R. Schlaf, N. R. Armstrong, B. A. Parkinson, C. Pettenkofer and W. Jaegermann, *Surf Sci*, 1997, **385**, 1–14.
38. Y. Su, M. A. Ebrish, E. J. Olson and S. J. Koester, *Appl Phys Lett*, 2013, **103**.
39. W. Zhang and K. Zhou, *Small*, 2017, **13**.
40. H. Jin, C. Guo, X. Liu, J. Liu, A. Vasileff, Y. Jiao, Y. Zheng and S.-Z. Qiao, *Chem Rev*, 2018, **118**, 6337–6408.
41. Y. Chen, K. Yang, B. Jiang, J. Li, M. Zeng and L. Fu, *J Mater Chem A Mater*, 2017, **5**, 8187–8208.
42. Y. Jia, J. Chen and X. Yao, *Mater Chem Front*, 2018, **2**, 1250–1268.
43. C. Tang and Q. Zhang, *Advanced Materials*, 2017, **29**, 1604103.
44. L. Sun, W. Zhou, Y. Liu, D. Yu, Y. Liang and P. Wu, *Appl Surf Sci*, 2016, **389**, 484–490.
45. X.-H. Tian and J.-M. Zhang, *J Magn Magn Mater*, 2019, **487**, 165300.
46. R. R. Nair, M. Sepioni, I.-L. Tsai, O. Lehtinen, J. Keinonen, A. V. Krasheninnikov, T. Thomson, A. K. Geim and I. V. Grigorieva, *Nat Phys*, 2012, **8**, 199–202.
47. L. Feng, J. Su and Z. Liu, *J Alloys Compd*, 2014, **613**, 122–127.
48. L. Sun, W. Zhou, Y. Liu, Y. Lu, Y. Liang and P. Wu, *Comput Mater Sci*, 2017, **126**, 52–58.
49. H. Wang, X. Zhao, Y. Gao, T. Wang and S. Wei, *Superlattices Microstruct*, 2018, **116**, 164–170.
50. W. Zhou, L. Dong, L. Tan and Q. Tang, *Nanotechnology*, 2021, **32**, 145718.
51. P. Giannozzi, S. Baroni, N. Bonini, M. Calandra, R. Car, C. Cavazzoni, D. Ceresoli, G. L. Chiarotti, M. Cococcioni, I. Dabo, A. Dal Corso, S. de Gironcoli, S. Fabris, G. Fratesi, R. Gebauer, U. Gerstmann, C. Gougoussis, A. Kokalj, M. Lazzeri, L. Martin-Samos, N. Marzari, F. Mauri, R. Mazzarello, S. Paolini, A. Pasquarello, L. Paulatto, C. Sbraccia, S. Scandolo, G. Sclauzero, A. P. Seitsonen, A. Smogunov, P. Umari and R. M. Wentzcovitch, *Journal of Physics: Condensed Matter*, 2009, **21**, 395502.
52. J. P. Perdew, K. Burke and Y. Wang, *Phys Rev B*, 1996, **54**, 16533–16539.

-
53. S. Grimme, *J Comput Chem*, 2006, **27**, 1787–1799.
 54. J. D. Pack and H. J. Monkhorst, *Phys Rev B*, 1977, **16**, 1748–1749.
 55. R. Almeida, A. Banerjee, S. Chakraborty, J. Almeida and R. Ahuja, *ChemPhysChem*, 2018, **19**, 148–152.
 56. D. Singh, S. Chakraborty and R. Ahuja, *ACS Appl Energy Mater*, 2019, **2**, 8441–8448.
 57. D. Chodvadiya, N. N. Som, P. K. Jha and B. Chakraborty, *Int J Hydrogen Energy*, 2021, **46**, 22478–22498.
 58. J. M. Gonzalez and I. I. Oleynik, *Phys Rev B*, 2016, **94**, 125443.
 59. M. Schlüter and M. L. Cohen, *Phys Rev B*, 1976, **14**, 424–431.
 60. A. Eftekhari and B. Fang, *Int J Hydrogen Energy*, 2017, **42**, 25143–25165.
 61. X. Wu, J. Han, Y. Feng, G. Li, C. Wang, G. Ding and G. Gao, *RSC Adv*, 2017, **7**, 44499–44504.
 62. N. Ran, B. Sun, W. Qiu, E. Song, T. Chen and J. Liu, *J Phys Chem Lett*, 2021, **12**, 2102–2111.